Combustion Science and Technology

ISSN: 0010-2202 (Print) 1563-521X (Online) Journal homepage: http://www.tandfonline.com/loi/gcst20

Characterization of a Nitrogen Diluted Hydrogen Diffusion Flame for Model Validation

Joseph A. Ranalli & Peter A. Strakey

To cite this article: Joseph A. Ranalli & Peter A. Strakey (2015) Characterization of a Nitrogen Diluted Hydrogen Diffusion Flame for Model Validation, Combustion Science and Technology, 187:9, 1351-1375, DOI: 10.1080/00102202.2015.1042102

To link to this article: http://dx.doi.org/10.1080/00102202.2015.1042102

Accepted online: 29 Apr 2015.

Combust. Sci. Technol., 187: 1351–1375, 2015
ISSN: 0010-2202 print / 1563-521X online
DOI: 10.1080/00102202.2015.1042102

Taylor & Francis
Taylor & Francis Group

CHARACTERIZATION OF A NITROGEN DILUTED HYDROGEN DIFFUSION FLAME FOR MODEL VALIDATION

Joseph A. Ranalli and Peter A. Strakey
National Energy Technology Laboratory, Morgantown, West Virginia, USA

Dilute hydrogen diffusion flames have been considered as a gas turbine combustion strategy that provides relatively low levels of NOx emissions for application in integrated gasification combined cycle power generation. These flames also represent a challenging environment for computational modeling efforts due to the complexity of molecular transport effects, turbulence-chemistry interaction, and near extinction flame conditions. In order to provide data for validation of computational modeling efforts, measurements of major species concentration and flame temperature were made in such a flame using spontaneous Raman scattering. Experimental results demonstrate the importance of differential species diffusion, which occurs due to the disparity between diffusion characteristics of hydrogen and nitrogen. Additionally, the flame temperatures observed were quite low relative to the equilibrium flame temperature, due to flame strain. This confirms the fact that suppression of the thermal mechanism of NOx formation plays a significant role in reducing NOx emissions from this type of flame.

Keywords: Hydrogen dilute diffusion; Raman spectroscopy

INTRODUCTION

Increasing awareness of the role of carbon dioxide (CO_2) as a greenhouse gas has placed pressure on the combustion research community to offer avenues for reduction in CO_2 emissions from combustion-based power generation systems. A significant research effort by the U.S. Department of Energy has been directed at investigation of integrated gasification combined cycle (IGCC) power configurations, which have the potential to provide power at near-zero levels of carbon emissions. The IGCC concept is based on the idea of using synthesis gas (syngas) derived from gasification of coal or biomass. Syngas consists primarily of hydrogen (H_2) and carbon monoxide (CO). This mixture can be preconditioned in the presence of water through a water-gas-shift reaction, resulting in a fuel mixture of only H_2 and CO_2, from which the carbon can be separated for subsequent sequestration. This leaves a high-hydrogen fuel available for use in power generation.

Besides the need for carbon reduction, an additional goal of the Department of Energy's Advanced Turbines Program is development of turbines capable of operation while emitting nitric oxides (NOx) at levels below 2 ppm @ 15% O_2. High-hydrogen fuels

Received 21 July 2014; revised 14 April 2015; accepted 14 April 2015.

Address correspondence to Joseph A. Ranalli, National Energy Technology Laboratory, Morgantown, WV 26507, USA. E-mail: jranalli@vt.edu
Color versions of one or more of the figures in the article can be found online at www.tandfonline.com/gcst.

like syngas represent a potentially troubling proposition regarding these goals due to the high flame speed of hydrogen in lean premixed combustion and high flame temperatures in diffusion flame combustion. Lean premixed combustion strategies are traditionally employed with natural gas fuels to minimize peak flame temperature, and thus, NOx formation. The higher flame speed of high-hydrogen fuels is known to introduce additional flame stabilization concerns in lean premixed configurations due to the increased potential for flashback. Work by the National Energy Technology Laboratory has considered the potential of using high-hydrogen fuels in a diffusion flame configuration, making use of nitrogen as a fuel diluent available from the gasification process's air-separation unit (ASU) in oxygen blown gasifiers as an alternate strategy to mitigate the high flame temperature and suppress NOx. For a typical bituminous coal, the nitrogen available from the ASU is roughly equal to the hydrogen produced by the gasifier on a volumetric basis.

A 50/50 H_2/N_2 mixture has an adiabatic, equilibrium stoichiometric flame temperature of 2025 K, which is still too high to avoid significant production of NOx via the thermal route (Weiland and Strakey, 2007b). Thus, in addition to nitrogen dilution, the strategy being considered makes use of extremely small, highly strained diffusion flames. This strategy limits the residence time in the flame region and promotes rapid reactant mixing, suppressing the flame temperature and avoiding high levels of thermal NOx formation. Several studies by Weiland et al. (2010) have considered the combustion performance of this configuration at both low and high pressures. Results from these studies indicate that sub-10 ppm NOx levels are possible. Figure 1 presents a set of NOx measurements made previously (Weiland and Strakey, 2009) for several different fuel injection velocities and fuel tube diameters as a function of coaxial air velocity. Previous experimental results were compared with computational fluid dynamics (CFD) studies that showed some success in predicting dilution effects on flame shape and stability (Weiland and Strakey, 2010). Optimizing this type of injector

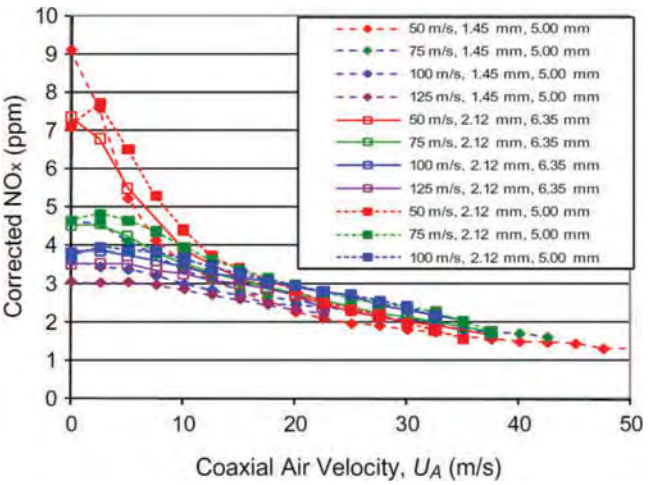

Figure 1 NOx emissions for various dilute-H_2 diffusion flame operating conditions. Legend represents varied fuel velocity, fuel inlet diameter, and air inlet diameter. Reprinted from Weiland, N.T., Chen, R.-H., and Strakey, P.A. 2011. Effects of coaxial air on nitrogen-diluted hydrogen jet diffusion flame length and NOx emission. *Proc. Combust. Inst.*, **33**(2), 2983–2989.

involves balancing the requirements of NOx level, injector pressure drop, and flame stabilization.

The potential issues of flame stabilization are caused by the relatively high fuel injection velocities (50–150 m/s) used to induce flame strain (Weiland and Strakey, 2007a). This is an area of ongoing research (Weiland and Strakey, 2009). One of the factors affecting stabilization is the preferential diffusion of hydrogen toward the lean side of the flame, resulting in localized regions of elevated equivalence ratio and temperature. The importance of these molecular transport effects and the complexity of the flame-turbulence interactions create a challenging environment for continued computational model development. Accurate computational models would enable greater physical insight into the chemical and physical phenomena underlying the flame stabilization and the suppression of NOx formation. Substantial experimental validation of models is required to provide this degree of fidelity.

While measurements of global NOx emissions, flame length, and flame stabilization behavior are valuable for design purposes, computational model validation requires more detailed measurements. There are several other experimental and theoretical studies of nitrogen-diluted hydrogen flames. Chen and Chen (1998) performed a theoretical analysis of laminar, nitrogen-diluted hydrogen flames, and showed that differential diffusion in these flames was dependent on the level of fuel dilution, with only a weak dependence on the strain rate. Chen and Chang (1998) conducted modeling studies of turbulent diffusion flames, and compared predicted differential diffusion results to the experimental results of Meier et al. (1996). Model results by Chen and Chang (1998) showed better agreement with the flame at far downstream locations, which they attribute to the laminarization of the flame in the near field region. Echekki et al. (2001) used a one-dimensional (1D) turbulence modeling approach that was able to describe the development of the jet, and predicted the importance of differential diffusion in the near field version of the jet flame.

In terms of experimental data, studies have produced validation data for these models. Barlow et al. (2000) made detailed measurements of scalar quantities within a $CO/H_2/N_2$ (syngas) jet flame at low strain. Their results showed that differential diffusion effects were washed out by the intensity of turbulent oscillations, though their measurements only began at an axial distance of 20 fuel jet diameters. Meier et al. (1996) studied nitrogen-diluted hydrogen flames using spontaneous Raman scattering to measure radial profiles of temperature and major species in the flame. They also employed a 50/50 mixture of hydrogen and nitrogen by volume for one of the flames studied. The results of Meier et al. (1996) showed average flame temperature very close to equilibrium values except for very low in the flame where "super-adiabatic" temperatures were observed on the lean side of the flame. They attributed this to differential diffusion in the laminar-like flame base. Previous studies have used experimental data from spontaneous Raman scattering to produce validation data in support of numerical modeling of turbulent H_2-N_2 flames (Neuber et al., 1998; Pfuderer et al., 1996). Additionally, extensive experimental flame data and model validation data, including turbulent jet flames, such as the one studied here, are available in the archive of the Turbulent Nonpremixed Flame (TNF) Workshop (http://www.sandia.gov/TNF/abstract).

The major difference between the existing data on hydrogen-nitrogen flames and the work presented here is in the flame strain rates. A first-order approximation of the global strain rate is U_f/D_f, where U_f is the fuel jet velocity and D_f is the diameter of the fuel tube. Of the H_2-N_2 flames employing a 50/50 mixture, the highest fuel jet velocity used was that of Neuber et al. (1998), who used an 8-mm fuel tube and a jet velocity of 46 m/s. This

corresponds to a strain rate of 5750 s^{-1}. Meier et al. (1996) also used an 8-mm fuel tube with a fuel jet velocity of 34.8 m/s resulting in a global strain rate of 4359 s^{-1}. With the 75 m/s velocity and 2-mm fuel tube used here, the global strain rate is calculated to be 37,000 s^{-1}, a factor of 6.4 higher than Neuber et al. (1998). The degree of strain has been reported to result in variations in the level of NOx production (Weiland and Strakey, 2009), along with challenges in stabilization of the flame under high strain rate. The detailed flame data at higher strain produced in this study may provide insight toward identifying the role that strain plays in their results, especially regarding the relationship between flame temperature, NOx formation, and strain rate.

Spontaneous Raman scattering is a laser-based diagnostic capable of measuring major species and temperature within a flame. This technique was applied to flames by members of the Combustion Research Facility at Sandia National Lab (Barlow et al., 1989). Spontaneous Raman scattering is an inelastic scattering effect in which the energy of a scattered photon is shifted by a quantized energy interaction with the scattering medium (Masri et al., 1996). Because each molecule has its own unique spectrum of vibrational and rotational Raman shifts, measurements of the spontaneous Raman scattering spectrum can be used to determine the composition of the flame. There are several experimentally challenging aspects of spontaneous Raman scattering. Crosstalk between the spectra from different species must be accounted for using data reduction techniques (Dibble et al., 1990). Chemiluminescence from the flame or other broadband light sources can contaminate the spectra, necessitating the use of high-speed shuttering. For example, a high-speed counter-rotating chopper was developed and described by Miles and Barlow (2000). Additionally, under extremely high laser pulse energy conditions, pulse stretchers have been used to reduce the peak power and reduce the potential for optical breakdown (Kojima and Nguyen, 2002).

In this study, we employed spontaneous Raman scattering to make measurements of major flame species and flame temperature. We also obtained measurements of the velocity field using particle image velocimetry (PIV) and of the reaction region via OH planar laser-induced fluorescence (PLIF) spectroscopy. These measurements provide a base set of data for development and validation of computational models and provide some insight into the physics of diluted hydrogen diffusion flames.

EXPERIMENTAL DETAILS

Dilute Diffusion Hardware

The experimental apparatus for the hydrogen dilute-diffusion combustion experiments was similar to that used by Weiland et al. (2011). The burner consists of a stainless steel tube that delivers a high velocity fuel jet. Surrounding this is a jet of coaxial air metered relative to the fuel at a global equivalence ratio of $\Phi = 0.50$. The flame is encircled by an 80-mm-diameter coflow of additional low-velocity air ($V = 0.15$ m/s) to over-ventilate the flame to a global equivalence ratio of 0.2 and to prevent the influence of room air currents. The original experiments of NOx emissions were made with a Pyrex enclosure around the flame to allow for global NOx emissions measurements. The application of high-power, focused laser diagnostics necessitated the removal of the Pyrex enclosure to prevent multi-photon ionization damage. The shielding influence of the coflow air was observed to prevent any changes to the flame structure as a result of unenclosed operation. A sketch of the burner is shown in Figure 2.

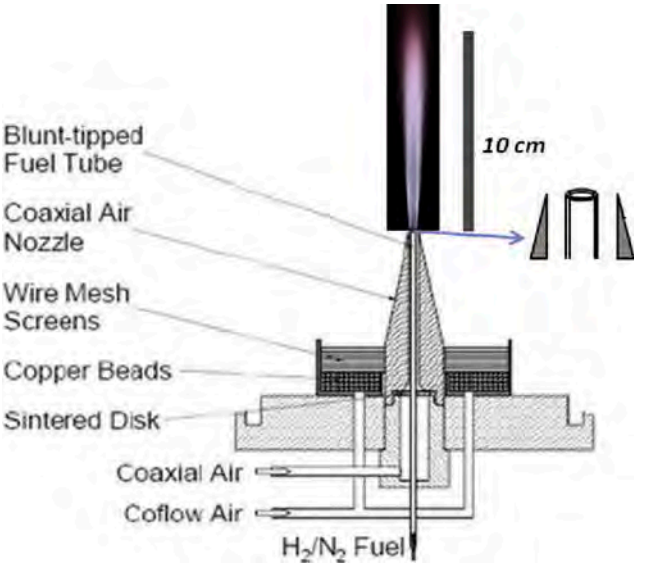

Figure 2 Sketch of the burner configuration under study.

Unlike previous studies that considered various geometries and operating conditions, the present study was focused on a single experimental configuration. For this study, the fuel jet had a diameter of 2.118 mm and the diameter of the air annulus was 6.35 mm. The fuel tube wall thickness was 0.53 mm. The fuel composition was 50%/50% by volume mix of high-purity hydrogen and nitrogen, metered at a rate of 15.45 SLPM. This flow rate corresponds to a fuel jet bulk velocity of 75 m/s. The fuel tube was sufficiently long to generate fully developed conditions at the jet exit with a Reynolds number of 5490 based on the bulk flow velocity and jet diameter. The dry, filtered coaxial air bulk velocity was 27 m/s. The coaxial air annulus was also sufficiently long enough to generate fully developed conditions at the exit with a Reynolds number of 5190 based on the bulk flow velocity and hydraulic diameter of the annulus.

OH PLIF Measurements

OH PLIF measurements were made to provide an indication of the flame length and the distribution of flame reaction region. The OH-PLIF system used a Spectra Physics Nd:YAG laser, that pumped a PDL-1 dye laser, whose output was frequency doubled to produce ~6 nsec duration, 30 mJ laser pulses at 10 Hz. Using the dye laser, the pulses were tuned to excite the Q1(9) line of the (1,0) band of the OH $A^2\Sigma - X^2\Pi$ electronic transition at 283.92 nm. This line is one of the strongest transitions present for OH and has only a weak temperature dependence over the range of temperatures expected in this flame.

A laser sheet was formed using an optical arrangement of fused silica cylindrical and spherical lenses. The laser sheet was approximately 125 mm high and 200 μm thick and was directed through the center of the burner. A Princeton Instruments PI Max intensified camera with a 1024×1024 pixel sensor was used to detect the OH fluorescence. A 45 mm *f*1.8 fused silica lens was used to collect the light. Long-pass and band-

pass filters were used to block scattered laser light and image only the fluorescence signal around 310 nm. Chemiluminescence measurements were also made using the same camera and filters. For both measurements, 200 images were collected and processed to yield ensemble averaged quantities.

PIV Measurements

An off-the-shelf 2D Particle Image Velocimetry system was used to make measurements of the dilute diffusion burner velocity field. The system used a NewWave Research Gemini dual-head PIV laser at 532 nm. An f = -25 mm cylindrical lens was used to form the beam into a sheet, and a 500 mm spherical focusing lens was used to focus the laser sheet on the burner centerline. The sheet thickness was measured to be about 200 μm at the beam waist. Scattering from the seed particles was detected using a TSI Powerview Plus camera with a 2048×2048 resolution and filtered to pass only the 532 nm light. The camera was set to a very small field of view (~7 mm) to provide adequate resolution using a 64×64 interrogation grid with 50% overlap. The resulting spatial bin size, and thus resolution, was 200 μm for axial locations from 0–31.5 mm. Further downstream the field of view was increased resulting in a resolution of 380 μm. The small field of view necessitated axial traversing of the burner such that each axial location was measured separately. Image acquisition and post-processing were performed using TSI's Insight software. At each axial location, 200 image pairs were collected and processed to yield mean and RMS values of axial and radial velocity.

The seed particulate used was 1 μm Yttrium-Stabilized Zirconia (YSZ) suspended in water to yield a thick slurry. Atomization of the slurry was performed with a TSI six-jet atomizer using either the nitrogen diluent or coaxial air producing droplets around 3 μm in diameter. The seeded flow then passed through a heated section of tubing to evaporate the water followed by a non-heated section to allow the flow to cool back to room temperature. The amount of water introduced into the flow increased the humidity by roughly 20%. Calculations of flame-speed, extinction strain rate, and flame temperature were performed with Chemkin and the additional humidity was found to have virtually no effect. When comparing with model data, users should use caution to ensure that comparisons with the reported PIV results compare the time-averaged mean velocity.

Single Shot Raman Spectroscopy Measurements

Experimental configuration. A frequency doubled Nd:YAG laser was used as a light source for Raman spectroscopy measurements. The laser produced 8 ns pulses at a frequency of 10 Hz. The pulse energy was around 1000 mJ at the 532 line. This high power was sufficient to cause laser-induced breakdown of the gases in the probe volume, so a pulse stretcher was employed to reduce the peak power. The design of the pulse stretcher followed Kojima and Nguyen (2002). The pulse stretcher consisted of a series of beam splitters and mirrors arranged into a three-cavity arrangement, with length ratios of approximately 1:2:4. Unlike Kojima and Nguyen, the shortest cavity was placed first in order to reduce clipping caused by beam divergence. The pulse stretcher arrangement is shown in Figure 3. The peak pulse power was reduced by roughly a factor of 10, stretching the pulse over approximately 100 ns.

After the pulse stretcher, two beam splitters in series were used to split off small fractions of the beam intensity for alignment and power sampling. One split beam was

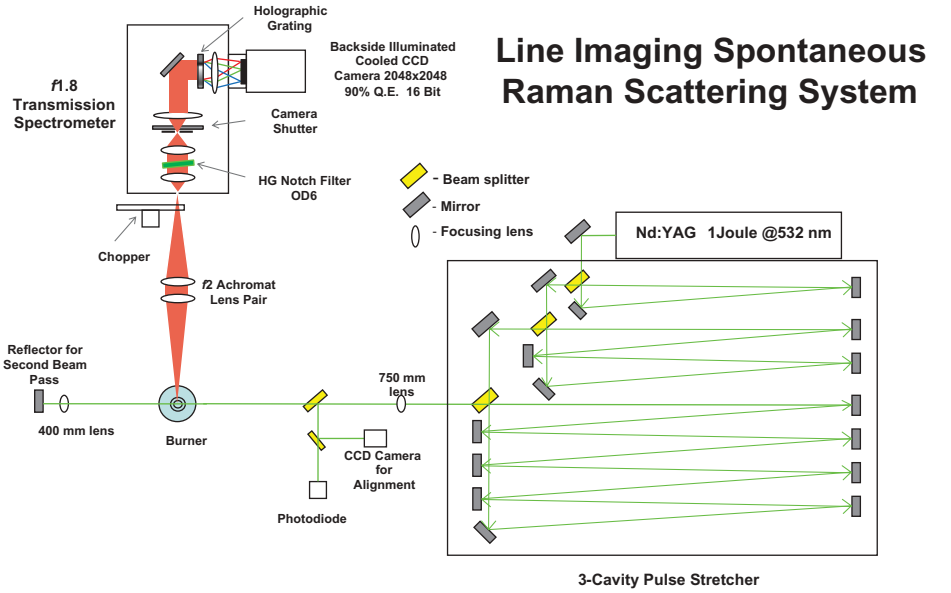

Figure 3 Top view sketch of the Raman spectroscopy experimental setup.

aimed at a CCD camera to allow alignment of the pulse stretcher. The second was detected by a photodiode, whose signal was measured using a box-car integrator, producing a measurement of the shot-to-shot laser intensity. A 750-mm focal length lens was used to focus the main portion of the beam into the burner probe volume. A mirror and a 400-mm focal length lens were used to retro-reflect and refocus the beam for another pass through the probe volume, effectively doubling the laser power. The probe volume had a beam waist of approximately 120 μm.

Scattering from the probe volume was collected using a pair of *f*2.0 achromat lenses that focused the light into a Kaiser Holospec *f*1.8 transmission imaging spectrometer with a magnification of 1. A holographic notch filter contained within the spectrometer removed the Rayleigh scattering at the laser wavelength. The spectrometer employed a broadband holographic transmission grating with a linear dispersion of 0.15 nm/pixel to produce a spectrum covering the range from 400 nm to 700 nm, providing both the Stokes and anti-Stokes Raman spectra in a single image. The spectrum was imaged by a Pixis 2048×2048 deep-cooled CCD camera. The camera had a 16-bit readout and 90% quantum efficiency employing backside illumination. The system was aligned to image a 16-mm segment of the laser beam. The resultant images contained the spatial coordinate in the vertical image dimension, with the horizontal dimension containing the spectrum. The 2048×2048 pixel images were binned by 8 pixels spatially and 4 pixels spectrally, to improve the signal-to-noise ratio. The resultant images had a resolution of approximately 0.6 nm spectrally and 107 μm along the beam path.

Experiments were performed with the room lights turned out to minimize the amount of stray light entering the spectrometer, but some stray light was still observed in the images. In addition, chemiluminescence from the target flame itself introduced broad-band spectral contamination. To minimize the amount of time that the CCD array

was exposed to these light sources, a dual shuttering system consisting of an external camera shutter and a rotating chopper was constructed. The camera aperture shutter was mounted within the spectrometer itself to reduce beam clipping. The optical chopper wheel was placed as close as possible to the spectrometer entrance slit. The chopper wheel was rotated at 6000 rpm with a 10-mm slit and the shutter was opened for a duration of about 8 msec. The shutter ensures that only one exposure occurs for every camera frame. The combination of shutters reduced the effective exposure time for stray light to around 120 μsec. This dual shuttering strategy is similar to that of Miles and Barlow (2000). In spite of these mitigations, final removal of these spurious light sources was conducted in post-processing as detailed in the Spectral Data Conditioning section.

Calibration methodology. The intensity of Raman scattering is linearly proportional to the number density of scattering particles. Given the spectral nature of this scattering, a Raman scattering measurement consists of the superposition of scattering from all species present in the probe volume. The methodology used in the present study is based on the crosstalk calibration matrix method described by Dibble et al. (1990). This approach condenses the spectrum from each specie into a single representative intensity, S_i. Since the spectral signatures of each specie are not completely independent, crosstalk is a possibility (that is, intensity from specie i may contribute to the observed signal of specie j). We can write the signal of each specie S_i (termed a superpixel) as the linear combination of the contribution from specie i, as well as all other species present:

$$S_i = \Omega \sum\nolimits_j c_{i,j}(T) N_j = \Omega \sum\nolimits_j c_{i,j}(T) \frac{x_j}{T} \tag{1}$$

The values $c_{i,j}(T)$ form the elements of the so-called crosstalk matrix. As indicated, these values are known to have some degree of temperature dependence. Calibration measurements were made to determine the values of these factors in a known flame environment. The scalar Ω represents the effects of characteristics of the optical collection and detection components. The absolute value for Ω was not measured in this study, rather all values are scaled relative to Ω as observed in the calibration measurements. Values of the superpixel boundaries used in this study are given in Table 1.

Calibration was performed using a McKenna style flat-flame burner. This type of burner was also used for calibration of Raman data by Meier et al. (1996). This premixed burner produces an approximately 1D flame stabilized on a porous disk with embedded water tubing for cooling. Surrounding the disk is a second flow passage through which an inert gas can be passed to reduce the influence of surrounding air on the flame. This burner type has been characterized in the literature for use as a temperature and equilibrium species calibration source while operating on propane (Sutton et al., 2006). We assume that the burner

Table 1 Superpixel wavelengths used for each species, including that for anti-Stokes nitrogen

Species	Wavelengths (nm)
N_2	600–613
O_2	574–584
H_2O	650–665
H_2	678–688
N_2 (AS)	467–483

characteristics are similar under the operating conditions chosen here. Though this type of burner is not adiabatic, heat loss is assumed to predominantly occur between the flame and the burner surface. This burner surface heat loss can be quantified by measuring a temperature difference in the water stream that is used to cool the porous plate. The calibration conditions used were chosen such that the measured value of heat loss to the burner surface was less than 10% of the total heat release rate. Equilibrium concentrations and flame temperatures were calculated using Cantera. The measured heat loss to the burner surface was included in the equilibrium calculation by subtracting the lost enthalpy from the mixture, rather than maintaining a strictly constant enthalpy. The Raman calibration measurements were made approximately 10 mm downstream of the flame front. Calculations using the Chemkin software package with finite rate chemistry showed that at this location the combustion products were very near equilibrium conditions. The uncertainty of temperature for this calibration results from the uncertainty of the flow rates (both gases and cooling water) and the water temperature measurements on which equilibrium conditions were based. The water flow rate was measured using a calibrated rotameter, and the water temperature measured using K-type thermocouples. The gas flows were metered using gas flow controllers (MKS Instruments) calibrated for the gases in question. Overall calibration flow rates are provided with the rest of the calibration conditions in Table 2. The sensitivities of the equilibrium temperature calculation to each parameter were evaluated and combined using error propagation. The uncertainties for the devices were: gas flows (air, hydrogen, and nitrogen) ±1%, cooling water flow ±2%, and water temperature thermocouples ±2.2°C. The resultant propagated uncertainty in equilibrium temperature for this calibration procedure was about ±30 K or roughly ±3%.

Calibration conditions must span the range of flame temperatures and must include all species expected to be present in the target flame. To simplify analysis, calibration conditions were carefully selected to limit the number of species present in a given flame. For example, rich flames create an environment free of oxygen, while lean flames are free of fuel (hydrogen). Example calibration spectra highlighting this difference are shown in Figure 4. Two calibration measurements were made at each calibration condition listed in Table 2. In addition, room temperature measurements of air, pure nitrogen, and a mixture of 98% nitrogen and 2% hydrogen were also included. These conditions allowed for the degree of crosstalk to be systematically determined. It was found that the only significant crosstalk term was that of hydrogen onto oxygen, yielding the following calibration matrix:

$$C(T) = \begin{bmatrix} c_{N_2}(T) & 0 & 0 & 0 \\ 0 & c_{O_2}(T) & 0 & c_{H_2 \to O_2}(T) \\ 0 & 0 & c_{H_2O}(T) & 0 \\ 0 & 0 & 0 & c_{H_2}(T) \end{bmatrix} \tag{2}$$

Table 2 Summary of McKenna burner conditions used for calibrations

Flame	Φ	% N_2	Total flow (SLPM)	Cooling H_2O (SCCM)	T_{ad} (K)	T_{corr} (K)
1	0.4	0	70	141	1427	1385
2	0.74	0	165	131	2079	1970
3	1.7	6	158	337	2069	1751
4	3.0	25.6	106.3	131	1409	1320
5	3.5	40.4	25	21	1124	1085

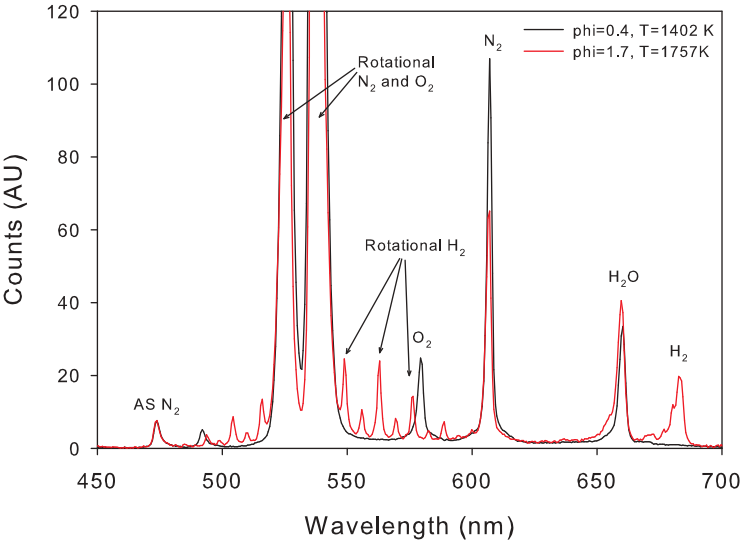

Figure 4 Sample of 100 shot average spectra from the calibration burner operating on hydrogen.

In order to determine the temperature functionality of the calibration matrix values, theoretical predictions made using RAMSES (Geyer, 2005) were scaled and offset as a best fit to the measured data. This provided a theoretical fit for the trends between the experimental calibration points. The results of this fit are shown in Figure 5. The calibration procedure also permitted the nitrogen Stokes/anti-Stokes ratio to be calibrated against temperature across the range of flame temperatures tested. An empirical fit was generated to calibrate between S/AS ratio and actual flame temperature.

The process of calculating species concentrations and temperature requires an iterative process. A guess for temperature is made, from which the calibration constants are estimated. The individual species number densities are then calculated based on this temperature guess according to Eq. (1). A new guess for the temperature is calculated by comparing the sum of the species number densities with the expected ideal gas number density at the guess temperature. This process was repeated until the guess temperature variation between iterations was reduced below a 0.01% threshold. It should be noted that

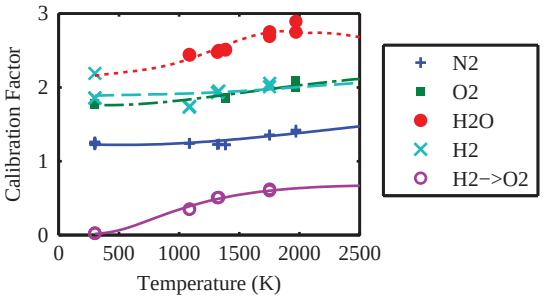

Figure 5 Calibration matrix element measurements as a function of temperature, compared with scaled and offset fits of the crosstalk behavior computed from RAMSES. (This figure was created using the software cited in Geyer, 2005.)

due to the relationship between molecular number density and mole fraction, this procedure is essentially identical to forcing the mole fractions to sum to a value of unity.

Because the mole fractions are made to sum to unity, the calculated mole fractions by species are primarily dependent on the relative ratio between superpixel intensities (differing from this only through the temperature dependence of $c_{i,j}$). The calculated ideal gas temperature, on the other hand, is primarily dependent on the absolute intensity of the given spectral image. The consequence of this characteristic of the processing methodology is that the species measurements have an inherent robustness. Slight misalignment of the optical system relative to the calibration was observed to alter the total accepted intensity, though it did not have a significant spectral dependence. Thus, while a correction (detailed in the next section) was necessary to produce consistent temperature measurements, the species calculations were much less sensitive to these experimental considerations.

Spectral data conditioning. Corrections to the data needed to be made for effects of vignetting, slit curvature, and stray light intensity. The complexity of the data conditioning needed to correct these effects warrants some further discussion. To calculate the species concentrations from a spectral image, the requisite data are superpixel intensity values for each specie, for each laser shot, and for each position in space along the imaging line. As day-to-day alignment of the laser and collection optics were not found to be absolutely repeatable, a correction for variations in the total collected intensity was applied by comparing the mean total intensity of the nitrogen peak in room air spectra measured each day. Shot-by-shot laser intensity (as measured by the beam sampler discussed in the Experimental Configuration section) was used to normalize the intensity of the spectrum image associated with each individual laser pulse. This produced spectra with a consistent number of data counts relative to the number of excitation photons.

Additional corrections were necessary to account for several optical characteristics of the spectrometer and imaging system. A sample image of the raw Raman spectrum acquired for air (N_2 and O_2) is shown in Figure 6. Two significant characteristics/aberrations are visible in this image. First, the spectral lines experience a shift in pixel space along the spatial (vertical) dimension, which we attribute to coma of the lens system. The second effect is decrease in intensity from the centerline outward, due to vignetting, which results from the large aperture optics used. To correct for coma, a separate pixel-to-wavelength calibration was calculated for each spatial location (image row) by applying a linear fit to the O_2 and N_2 centerline pixel values measured in a room air spectrum. These multiple calibrations were used to generate separate superpixel bin boundaries for every spatial location. After superpixel boundaries were determined, a spatial vignetting

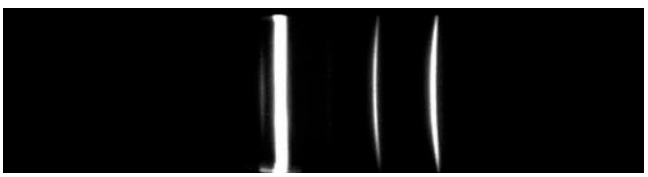

Figure 6 Sample spectrum taken of dry room air, showing the spatial effects of coma and vignetting. The three major features visible in the spectrum are from left-to-right: (1) rotational N_2 and O_2 scattering adjacent to the laser line, (2) vibrational O_2, (3) vibrational N_2.

correction was calculated to flatten the known room air spectrum nitrogen peak across all spatial locations. While this does correct for the shift in the mean intensity due to vignetting, it should be noted that this correction does not overcome the signal-to-noise degradation that occurs due to the lower peak intensity at the edges of the imaging region. A separate room air spectrum was collected every time changes were made to the imaging system alignment to ensure that these corrections were as closely referenced as possible to any particular data set.

This process produced a set of images from which all superpixel boundaries were known at all spatial locations and in which all spatial locations share reference intensity values with the calibration tests. However, while the chopper and shuttering system discussed in the Experimental Configuration section provided significant reductions in the level of chemiluminescence and other stray light detected, it was not possible to completely eliminate all sources of spurious signal. Therefore, several strategies were employed to remove the broad-band background from the spectra.

Calibration measurements were made downstream of a laminar, flat flame. At each condition an image set was acquired with the laser inhibited to produce an image of the background chemiluminescence spectrum. This was directly subtracted. A small amount of broadband light, only present during laser operation, was still observed even after chemiluminescence subtraction. Tests using argon to eliminate the Raman scattering signal confirmed that this broadband light was a result of stray laser light and was not a component of the actual Raman signal. A spectrum featuring only Raman scattering by nitrogen was used to generate a polynomial fit for this additional background, and was also subtracted. The end result of this processing was a spectrum that contained no background save the actual intensity associated with the Raman scattering. From this, integrated superpixel intensities were obtained.

Due to the turbulent oscillations of the flame front in the diffusion flame studied here, the location of chemiluminescence within the measurement region was not constant and steady measurements of the background light intensity were not possible. Therefore, a different method had to be used to produce a flattened spectrum. The spectral shape of the chemiluminescence background was observed to be consistent even as the flame front moved, varying only in absolute intensity. A single prototype background curve was obtained by averaging several flame images together. This prototype spectrum was scaled individually for each spatial location and each laser-shot image. Scaling was performed by comparing the prototype and measured intensities in a region known not to contain any Raman scattering (615–620 nm). Subtraction of the scaled chemiluminescence curve was observed to remove all broad-band background signals from the data. Superpixel intensities were then measured from this flattened spectrum, as in the calibration processing. The representative superpixel intensities were then used to calculate composition and temperature, as described in the previous section.

RESULTS

A sample Raman spectrum with all processing applied is shown in Figure 7. The superpixel bin boundaries are also shown in this figure. Understanding this spectrum is instructive in interpretation of the Raman spectroscopy data. The vertical dimension in the image represents the 1D spatial coordinate along the laser probe volume as it cuts through the flame centerline 5.5 mm above the burner nozzle. At roughly the vertical centerline of the image, Raman scattering is clearly visible at wavelengths associated with hydrogen

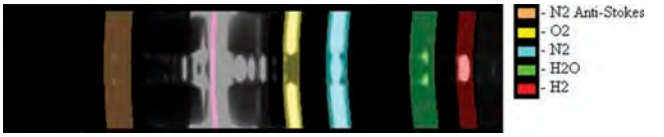

Figure 7 Sample spectrum of the dilute diffusion flame with spatial corrections and background subtraction applied. Spectrum is an average of 100 shots taken at 5.5 mm axially from the nozzle. Horizontal dimension is wavelength and vertical dimension is spatial distance along the laser probe length. Color overlays show the calculated bin locations for each specie. Fuel is indicated along the centerline with air bounding it on the top and bottom. Water (indicating reaction) is present in the interface.

and nitrogen, representing the 50/50 H_2/N_2 fuel mixture. Near the top and bottom of the image, two regions are present where the scattering reflects the presence of O_2 and N_2 (that is, air), with all other species absent. Two interface regions between the fuel core and the surrounding air are the flame front. Within the flame front, H_2O scattering is clearly present indicating the presence of reaction products. Additionally, in the flame region we observe an increase in N_2 anti-Stokes scattering indicating the higher energy states populated due to higher temperatures in the reaction region. High temperature is additionally reflected in the suppressed N_2 intensity in the flame region that may be attributed to the reduced scattering species density. The spatial superpixel intensities from this spectrum are presented in Figure 8, graphically showing the features of the previous description. Figure 8 is a radial plot of temporally averaged superpixel intensity through the centerline of the burner, which corresponds to the center of the image in Figure 7. This plot shows the basic features of the flame, including the fuel, oxidizer, and reaction zones.

The precision of the Raman measurements was estimated using the calibration data. The calibration flames represent a steady, uniform target for measurement. Standard deviations were calculated from the calibration data using 200 laser shots, giving an indicator of the precision of the measurement, without comment as to the actual accuracy. Intuitively, it was observed that the uncertainty estimated in this manner depended primarily on the total signal-to-noise in the images. Thus, increases in temperature increased the species uncertainty at a fixed concentration by reducing the total Raman intensity [see Eq. (1)]. The only case in which this trend is not followed is calculation of the temperature by Stokes/anti-Stokes ratio of nitrogen, because the anti-Stokes scattering does not significantly occur at low temperatures. Besides temperature dependence,

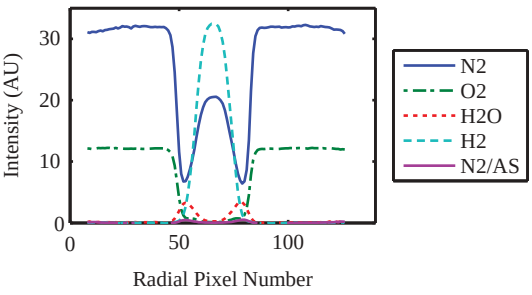

Figure 8 Spatial superpixel intensities measured from the sample spectrum in Figure 7. Values reflect the average of 100 shots at 5.5 mm axially above the burner tip.

Table 3 Peak RMS uncertainty for each Raman measured quantity

Quantity	Max RMS	Mean RMS
T (ideal gas)	66.8 K	30.4 K
T (N_2 ratio)	231 K	89.0 K
N_2	0.019	0.009
O_2	0.014	0.007
H_2	0.016	0.010
H_2O	0.010	0.005

uncertainty was also greater for measurements with low mole fractions due to their corresponding low intensity. Likewise, the radial vignetting effect described in the Spectral Data Conditioning section, also caused uncertainty to increase toward the edges of the image. The boundary of "the edges" relative to vignetting was observed as beyond approximately 4 mm in radius. Numerical values for the mean and maximum RMS for each variable are given in Table 3. A plot showing actual precision bands for a sample measurement condition, showing the spatial variation in the temperature uncertainty, is given in Figure 9. Describing the spatial variation, the standard deviations for mole fractions were observed to be less than 0.01 at the centerline and gradually rose to a maximum value always less than 0.02 at the outer edge of the reaction zone. For the ideal gas temperature calculations, the standard deviation was less than 40 K in the cool center of the jet, then rose to around 65 K at the peak temperature zone, before falling back to 40 K at the outside edge of the flame region and then slowly rising to 100 K at the extreme outer edge of the measurement zone (6 mm). A single value is more difficult to state for the Stokes/anti-Stokes temperature due to the increase in uncertainty at low temperatures. Generally the Stokes/anti-Stokes uncertainty in the region of peak flame temperatures was around 150 K.

In calculating statistics for the data, means and standard deviations were calculated as a function of radial position for several axial distances from the nozzle tip. A total of 200 spectra were collected at each axial position, from which profiles of mean value and standard deviation were computed. Since the line imaging approach used here captured the entire width of the flame region, the two "halves" of the data were then "folded" about the flame centerline and averaged, creating radial profiles. Averaging the standard deviation

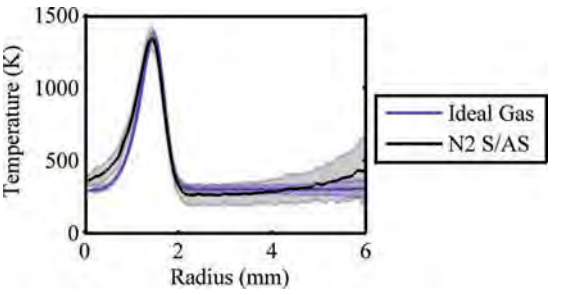

Figure 9 Sample plot of Raman results for both temperature calculation methods at an axial location of 5.5 mm. Solid lines are the mean value and shaded bands show measurement precision at a level of +/- one standard deviation.

calculations by flame-half is justified in that it allows the standard deviation to contain only the change in a quantity about its mean as a result of turbulent fluctuations. The approach not chosen (calculate standard deviation relative to the already folded radial mean profile) has the undesirable consequence of including both effects of turbulence and asymmetry.

Measurements were made at a series of axial positions referenced to the tip of the nozzle: 5.5 mm, 15.5 mm, 31.5 mm, 51.5 mm, and 71.5 mm. Measurements closer to the base of the jet were limited by laser scattering from the tip of the nozzle. The data are shown in Figures 10 to 13. Radial profiles of mean species concentrations are shown at each axial location in Figure 10, with mean temperature data for all axial locations shown in Figure 11. Likewise, measurement standard deviations for mole fraction at all locations are shown in Figure 12 with the corresponding temperature standard deviations shown in Figure 13. Relative to the precision of the measurement discussed previously, mole fraction standard deviations above the uncertainty of 0.015 are significant within a radius of 4 mm, likewise for temperature standard deviations above the uncertainty of 100 K. The accuracy of the Raman calibration can be estimated based on mean measured values in the two regions with known composition. The comparison in Table 4 indicates that the mole fractions in both the fuel and air regions produce results relative to their known values within ±0.01.

The trends observed from the means (Figures 10 and 11) support the expected behavior for measurements made in a turbulent jet flame. Near the attachment point, the flame behaves in a nearly laminar manner due to the low velocity behind the blunt end of the fuel tube and the increased viscosity due to the high temperatures. In this region lies a narrow, relatively stationary flame zone. The boundary between the fuel and air jets near the nozzle may also be observed in the gap in the mean axial velocity profiles at the radial location of 1.5 mm, which corresponds to the outer edge of the fuel tube, as shown by the PIV data in Figure 14. As the measurement location moves downstream, the time averaged flame region, which can be taken to be the region of water formation in Figure 10 or high temperature in Figure 11, becomes wider due to turbulent mixing, until reaching the tip of the flame, at which point very little fuel remains unburned. The degree of turbulence can be taken from the RMS axial velocity profiles in Figure 14, which show a broadening of the profile and an overall increase in value with increasing distance from the burner tip. These observations may be compared with the instantaneous and time-averaged OH PLIF measurements shown in Figure 15, which show the same flame behavior. The instantaneous OH PLIF images indicate that the apparent widening of the mean flame region may be attributed primarily to turbulent movement of the thin flame surface, rather than a true broadening of the flame surface itself.

To assess the degree to which flame motion impacts the oscillations in the local value, it may be instructive to consider the standard deviation plots in Figures 12 and 13. Near to the burner tip, the standard deviations of temperature and water (here representing reaction progress) exhibit a bimodal distribution. Due to the sharp gradients associated with the edges of the instantaneous flame front, small movements of the flame relative to the mean location of these gradients causes dramatic changes in the local, instantaneous measurement. Thus, the high standard deviations in those regions are not necessarily indicative of a high variability in the reaction itself, but rather the gross flame front motion. The temperature data shown in Figure 13 indicate a maximum standard deviation of around 265 K. We may remove the effects of flame surface motion by tracking the shot-to-shot maximum measured temperature at any radial position (i.e., considering peak

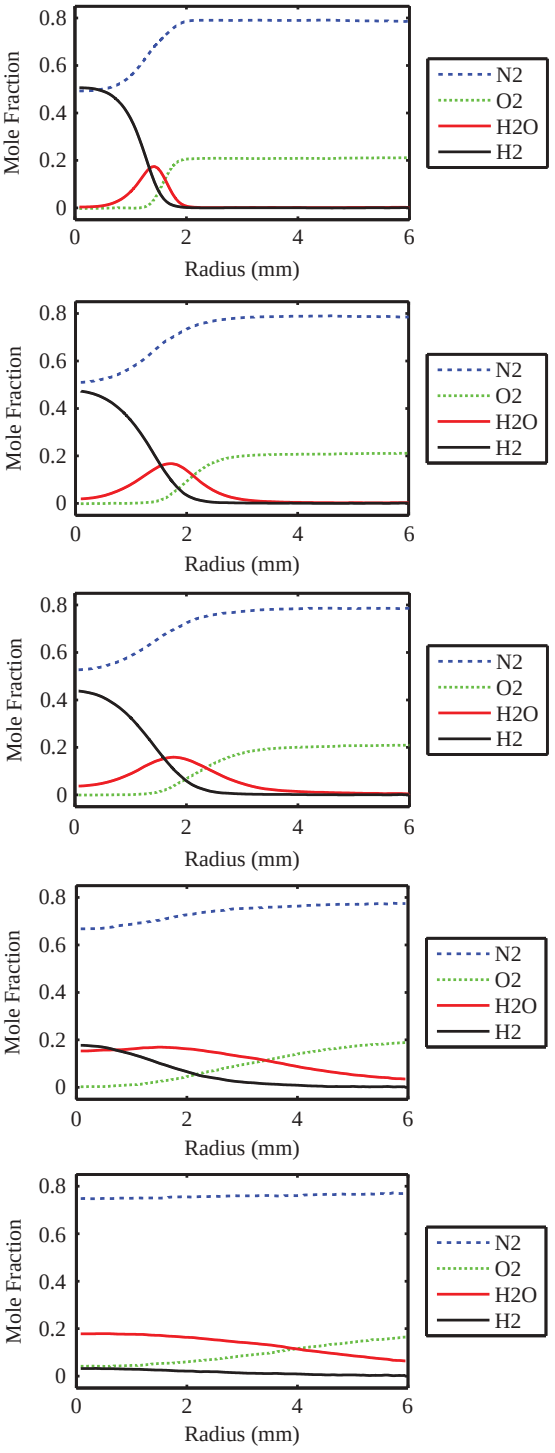

Figure 10 Radial profiles of species mole fractions measured in the flame. Axial positions are (top to bottom): 5.5 mm, 15.5 mm, 31.5 mm, 51.5 mm, and 71.5 mm. All posititons were measured from the nozzle.

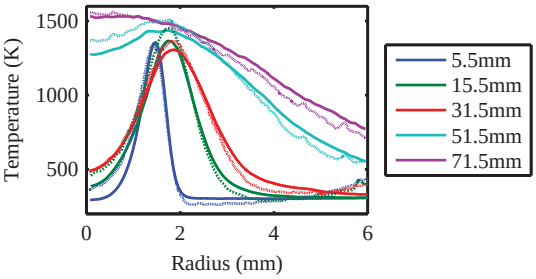

Figure 11 Temperature profiles at several axial locations. Solid lines: ideal gas calculation; dashed lines: Stokes/anti-Stokes nitrogen ratio calculation.

temperature irrespective of its radial position). In that case the observed peak temperature standard deviation is only around 103 K. This suggests that close to the nozzle tip, the fluctuations in measured quantities are primarily caused by bulk motion of the flame front relative to the spatial coordinate, while remaining otherwise stable. At downstream locations, the bimodal distribution ceases to be visible as the sharp gradients cease to be present in the mean profiles.

The discrepancy between peak temperature and the mean temperature profiles can be further analyzed by Table 5, which provides the mean and standard deviation values of peak radial temperature (neglecting flame surface motion in space). These values further confirm that the values of the mean radial profile in Figure 11 are artificially reduced due to the averaging operation. Even when neglecting the flame surface motion effect, the peak flame temperatures observed are all relatively low compared to the stoichiometric adiabatic flame temperature for this fuel (2025 K). This provides an explanation for the low NOx produced by these flames (Figure 1).

One notable feature observed in the mean radial profiles in Figure 10 is that the time-averaged hydrogen and oxygen zones overlap at all of the axial locations. This occurrence has significant implications as to identifying the physics of the turbulence-flame interactions at work and whether a kinetic-limited or mixing-limited reaction mode takes place in these regions. As the average values in Figure 10 do not describe the actual simultaneity of occurrences, it is convenient to compare the instantaneous mole fractions of hydrogen and oxygen as in Figure 16. A mixing limited diffusion flame would show points clustered around the axes and the origin, resulting from the case where all mixed air and fuel react to completion instantaneously. In the actual data we observe that, near the burner tip (5.5 mm), the data is scattered over a range of oxygen and hydrogen mole fractions, indicating that both unburned hydrogen and oxygen are simultaneously present in some instances. For clarity, only every fifth data point is plotted. This presence of mixed, but unburned reactants signifies incomplete combustion of the reactant mixture, which we attribute to slow local reaction rates relative to the jet velocity. That is to say, the reaction near the burner tip is kinetically limited to some extent.

As we move downstream to 31.5 mm, the densest part of the curve shifts closer toward the origin of the plot, corresponding to more complete reaction of the fuel-air mixture. However, we also notice an increase in the density of scattered data points that occur to the upper right region in the plot. These points indicate pockets with high concentrations of both reactant species. A second plot of this data is shown in Figure 17 with data colored by temperature. From Figure 17 it is clear that the scattered points

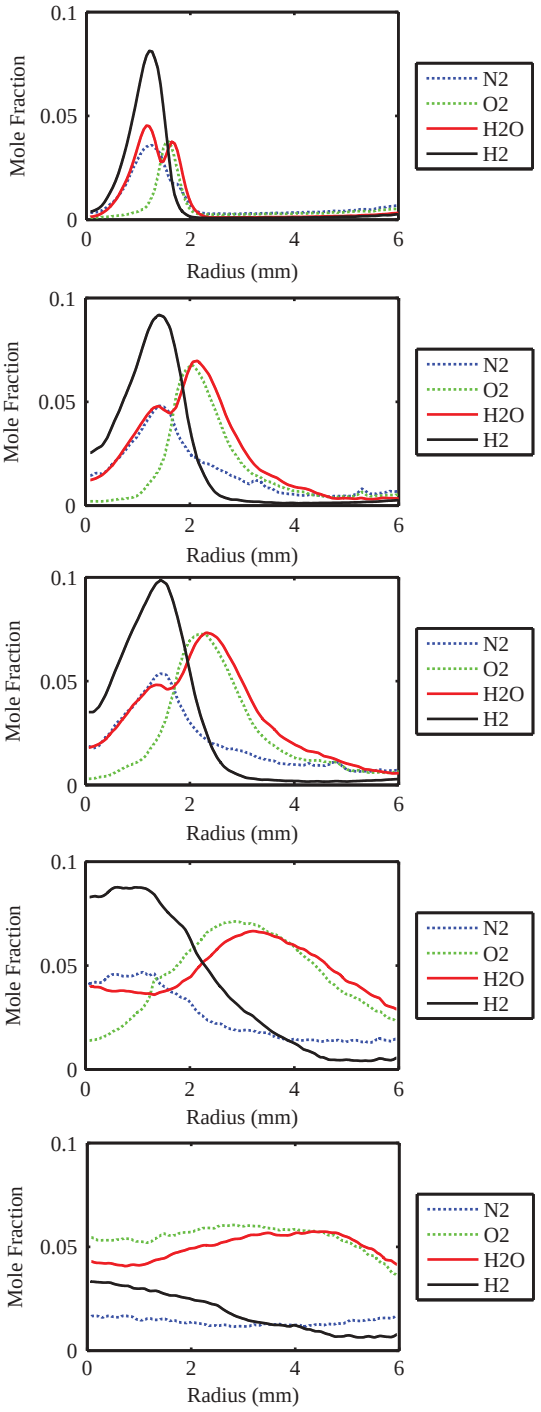

Figure 12 Radial profiles of standard deviation of species mole fractions measured in the flame. Axial positions are (top to bottom): 5.5 mm, 15.5 mm, 31.5 mm, 51.5 mm, and 71.5 mm. All posititons were measured from the nozzle.

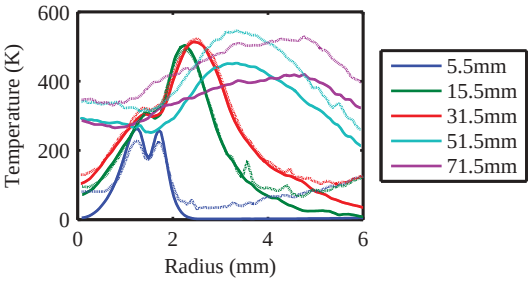

Figure 13 Standard deviation in temperature profiles at several axial locations. Solid lines: ideal gas calculation; dashed lines: Stokes/anti-Stokes nitrogen ratio calculation.

Table 4 Calculated mole fractions in the regions with known composition

	Room air		Fuel jet	
Quantity	Known	Measured	Known	Measured
N_2	0.79	0.787	0.50	0.493
O_2	0.21	0.211	0.00	0.003
H_2	0.00	0.000	0.50	0.506
H_2O	0.00	0.002	0.00	–0.003

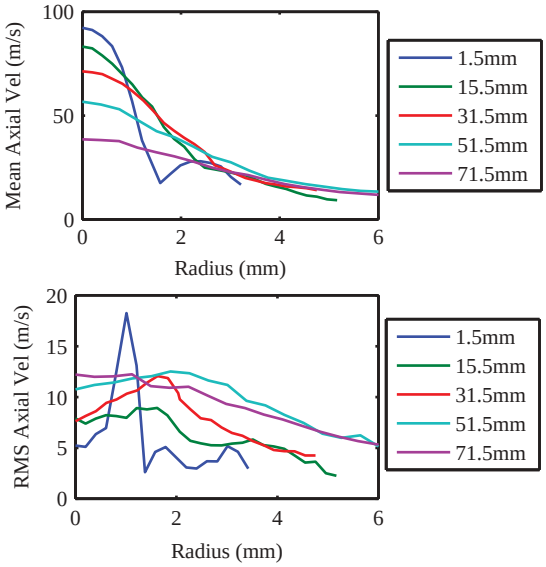

Figure 14 PIV measurements of mean (top) and RMS (bottom) axial velocity at varying locations from the burner tip.

containing both reactant species also frequently correspond to conditions where a low temperature (less than 1000 K) is observed. The minimum temperature at extinction can be assessed using a laminar, opposed flow burner calculation, such as that in CHEMKIN. For this calculation a detailed hydrogen-air mechanism was used (Li et al., 2004) and the

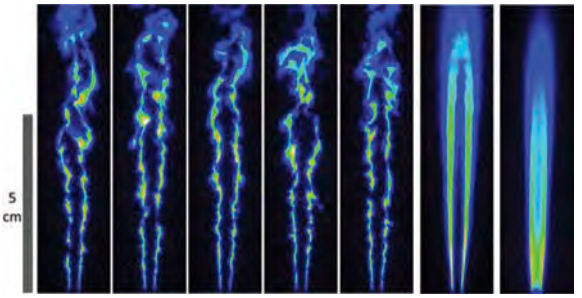

Figure 15 Snapshots of OH PLIF measurements as well as an OH* chemiluminescence snapshot. Left-to-right: Five individual frames from the OH PLIF data, followed by an average OH PLIF image, and last mean OH* chemiluminescence.

Table 5 Mean and standard deviation of the peak radial temperature at each axial location

Axial Pos	T_{max} (K)	T_{stddev} (K)
5.5 mm	1510	103
15.5 mm	1702	147
31.5 mm	1701	150
51.5 mm	1832	162
71.5 mm	1819	156

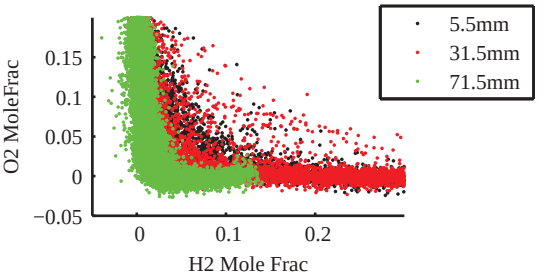

Figure 16 Comparison of hydrogen and oxygen presence on a shot-by-shot basis.

burner velocity was gradually increased until extinction occurred, as shown in Figure 18. The last data point in the plot, at a strain rate of 21,000 s^{-1} corresponds to near-extinction conditions with a resultant peak flame temperature of 1325 K. Many of the instantaneous temperatures shown in Figure 17 are below the extinction temperatures of 1325 K for this reactant mixture. We therefore consider the points exhibiting low temperature and relatively high concentrations of mixed reactants to be evidence of local extinction of the reaction. This localized extinction can also be seen in the instantaneous OH PLIF images in Figure 15. Gaps are present in the reaction region as indicated by the instantaneous OH fluorescence, which implies that the reactants are present and mixed, but are only partially reacted. The increased likelihood of unburned reactants being present simultaneously

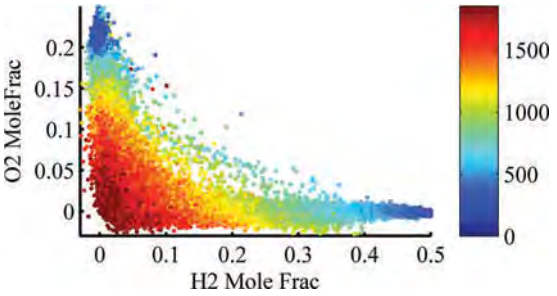

Figure 17 Comparison of hydrogen and oxygen on a shot-by-shot basis, colored by temperature.

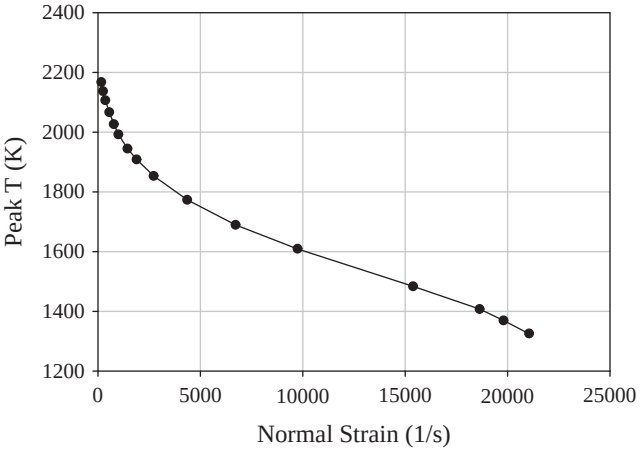

Figure 18 Temperature as a function of strain rate as calculated using CHEMKIN for an opposed flow laminar diffusion flame burning a 50/50 mixture of N_2 and H_2 at reactant inlet temperatures of 300 K.

(Figure 16) at axial locations of 31.5 mm and less corresponds qualitatively with the axial position of the gaps observed in the OH PLIF images (Figure 15).

Measurements at axial locations of 51.5 mm and 71.5 mm no longer exhibit unburned fuel-air mixtures resulting from local extinction or otherwise. The corresponding mole fraction comparison curve in Figure 16 shows data points that occur only near the origin (indicating reactants have been consumed) or along the coordinate axes (indicating fuel or oxidizer is present without having been mixed). The fact that some hydrogen is still present indicates that portions of the unburned fuel core penetrate into the flame brush at these axial locations. It is significant, however, that these fuel pockets are never present together with oxygen, indicating that by this point in the flame all reactions made possible by sufficient mixing have already occurred. Referring to Figure 17 we see that this near-origin region also corresponds to the highest temperatures in the flame, providing an explanation for these faster reactions. From these observations, we may infer that within the flame brush, the flame may be said to be completely mixing dominated. These observations may help to guide the choice of a combustion modeling approach for computational efforts.

One effect that was expected in this flame is the occurrence of differential species diffusion. A possible way to assess the presence of this effect is by considering the temperature as a function of mixture fraction. Mixture fraction is calculated as:

$$f_i = \frac{Z_i - Z_{i,coax}}{Z_{i,fuel} - Z_{i,coax}} \tag{3}$$

where Z_i represents the elemental mass fraction of either H or O atoms. In the absence of molecular transport effects, the mixture fraction based on either H or O atoms should be exactly equal. It is possible to calculate an adiabatic equilibrium flame temperature as a function of mixture fraction, by assuming a given fuel mixture (in this case 50% H_2, 50% N_2). Differential diffusion would have the effect of causing the assumption about fuel mixture ratio to be invalid. That is, if hydrogen diffuses faster than nitrogen, we might expect to find a local effective fuel mixture of 60% H_2, 40% N_2. Due to the low mass of hydrogen, this change would have the effect of causing a decrease in f_O and an increase in f_H. Thus, the plots of mixture fraction would develop apparent skews in opposite directions if differential diffusion is present but not accounted for under the assumed adiabatic equilibrium curves. Plots of mixture fraction that exhibit superadiabatic flame temperatures may be said to be evidence that the local fuel mixture does not correspond to the mixture at the fuel injector (50/50 H_2/N_2), or that the two components of the fuel diffuse at different rates.

Plots of the mixture fraction based on both H (right-hand column) and O (left-hand column) atoms at all axial locations are shown in Figure 19. Adiabatic equilibrium calculations are indicated by the solid line with a stoichiometric mixture fraction occurring at $f_{O,H} = 0.3$. For the 5.5-mm case, a significant skew is clearly visible in the oxygen mixture fraction, resulting in superadiabatic flame temperatures on the lean side ($f_{O,H} < 0.3$). This is caused by regions of effectively rich stoichiometry. These temperatures indicate that the actual fuel mixture present on the lean side is not 50/50 nitrogen/hydrogen mixture, but a mixture in which hydrogen concentration is increased by differential diffusion. The effects of differential diffusion are largely overcome by the effect of turbulent mixing by 51.5 mm. The occurrence of differential diffusion has great importance to modeling of this type of flame, especially insofar as it occurs in the laminar-like region near the base of the flame where it is expected to play a role in flame stabilization. Many combustion modeling approaches are based on a unity Lewis number assumption (Le = α/D), or at least a constant assumed Lewis number. This assumption will not allow for superadiabatic temperature and the associated localized increase in reaction rates. This limitation could have a pronounced effect on flame stabilization as well as pollutant formation.

CONCLUSIONS

A comprehensive set of data were acquired to characterize a diluted hydrogen diffusion flame with potential applications to low-NOx IGCC combustion. Data available are radial velocity profiles (obtained via PIV), radial profiles of major species and temperature (obtained via Raman spectroscopic measurements), and images of the flame reaction region (obtained from OH PLIF). Several behaviors revealed by these data make this an interesting target flame for computational model development and validation. Beginning at the attachment point, the flame initially has a laminar-like character, resulting in a relatively thin reaction zone. The high degree of strain in this region creates a

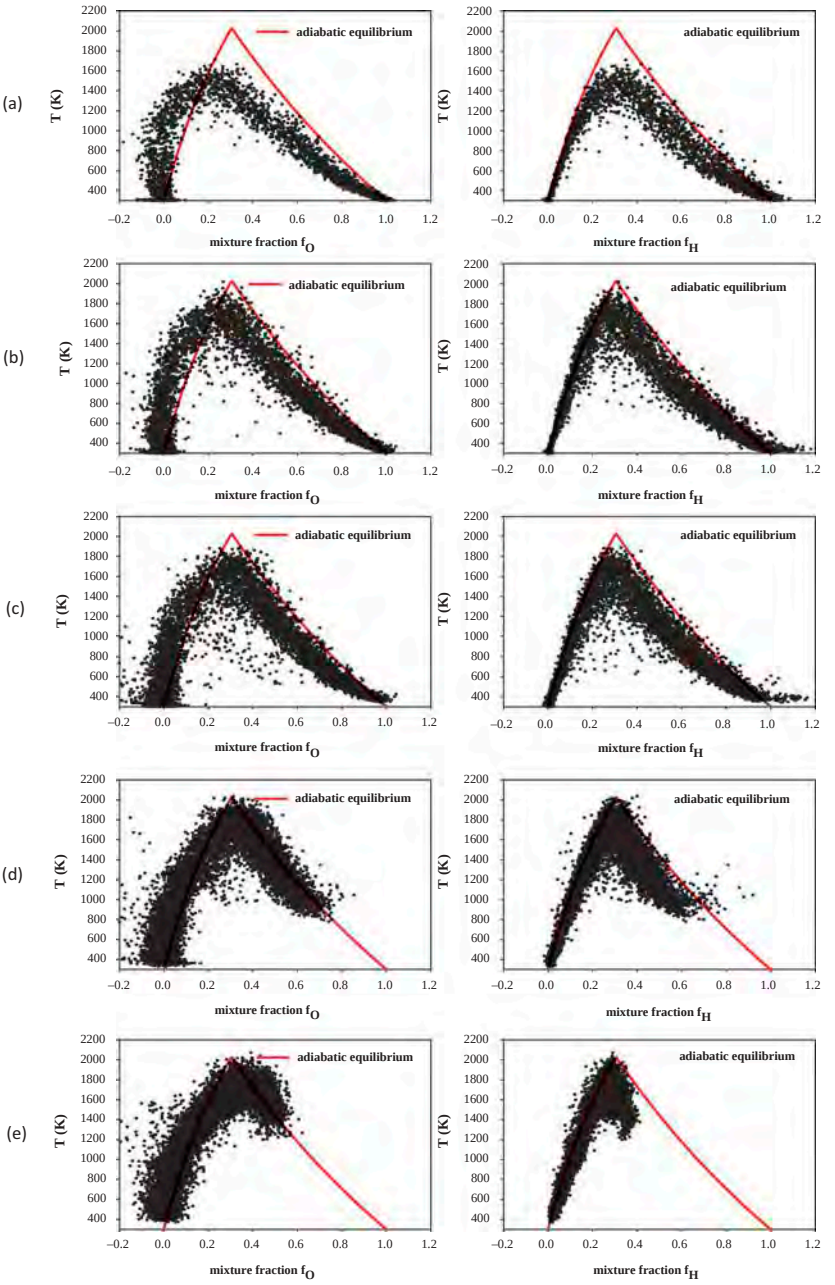

Figure 19 Mixture fractions calculated for Raman data at axial locations of (a) 5.5 mm, (b) 15.5 mm, (c) 31.5 mm, (d) 51.5 mm, and (e) 71.5 mm. Note the super-adiabatic flame temperatures indicated in the oxygen mixture fraction calculation.

reduction in flame temperature significantly below the adiabatic, leading to a reduced level of thermal NOx formation. Localized extinction events were observed in the OH PLIF data in this region and were corroborated with reactant species observations.

Differential diffusion effects are observed to play an important role in the region of the flame nearby to the attachment point where mean velocity and turbulence levels are low, indicating the potential for a strong influence of differential diffusion on the flame stabilization process. Moving downstream within the flame, turbulent oscillations were observed to play a stronger role, resulting in an increased degree of mixing, and bulk movement of the flame surface. This was observed by an increased width in the mean temperature and species profiles. Local extinction events ceased to occur at axial locations greater than about 30 mm and combustion within the flame brush could be said to be mixing-limited, in that no unburned fuel-air mixtures were observed in the Raman data.

Both the interesting phenomena observed in this particular flame and its potential to serve as a low-NOx combustion strategy make it an attractive avenue for further experimental investigation and advanced computational model validation and development.

ACKNOWLEDGMENTS

This report was prepared as an account of work sponsored by an agency of the United States Government. Neither the United States Government nor any agency thereof, nor any of their employees, makes any warranty, express or implied, or assumes any legal liability or responsibility for the accuracy, completeness, or usefulness of any information, apparatus, product, or process disclosed, or represents that its use would not infringe privately owned rights. Reference herein to any specific commercial product, process, or service by trade name, trademark, manufacturer, or otherwise does not necessarily constitute or imply its endorsement, recommendation, or favoring by the United States Government or any agency thereof. The views and opinions of authors expressed herein do not necessarily state or reflect those of the United States Government or any agency thereof.

NOMENCLATURE

S_i	scattering intensity for species i
C	cross-talk calibration matrix
T	temperature
N	number density
x	mole fraction
f	mixture fraction
Z	atomic mass fraction
Φ	equivalence ratio
T_{ad}	adiabatic flame temperature
T_{corr}	flame temperature corrected for heat loss to the calibration burner surface

REFERENCES

Barlow, R.S., Dibble, R.W., and Lucht, R.P. 1989. Simultaneous measurement of Raman scattering and laser induced OH fluorescence in nonpremixed turbulent jet flames. *Optics Lett.*, **14**(5), 263–265.

Barlow, R.S., Fiechtner, G.J., Carter, C.D., and Chen, J.-Y. 2000. Experiments on the scalar structure of turbulent $CO/H_2/N_2$ jet flames. *Combust. Flame*, **120**(4), 549–569.

Chen, J.-Y., and Chang, W.-C. 1998. Modeling differential diffusion effects in turbulent nonreacting/reacting jets with stochastic mixing models. *Combust. Sci. Technol*., **133**, 343–375.

Chen, Y.-C., and Chen, J.-Y. 1998. Fuel-dilution effect on differential molecular diffusion in laminar hydrogen diffusion flames. *Combust. Theor. Model*., **2**, 497–514.

Dibble, R., Starner, S., Masri, A., and Barlow, R. 1990. An improved method of data acquisition and reduction for laser Raman-Rayleigh and fluorescence scattering from multispecies. *Appl. Phys. B*, **51**(1), 39–43.

Echekki, T., Kerstein, A.R., Dreeben, T.D., and Chen, J.-Y. 2001. 'One-dimensional turbulence' simulation of turbulent jet diffusion flames: Model formulation and illustrative applications. *Combust. Flame*, **125**, 1083–1105.

Geyer, D. 2005. 1D-Raman/Rayleigh experiments in a turbulent opposed-jet. PhD thesis. TU Darmstadt, Düsseldorf, Germany.

Kojima, J., and Nguyen, Q.-V. 2002. Laser pulse-stretching with multiple optical ring cavities. *Appl. Opt*., **41**(30), 6360–6370.

Li, J., Zhao, Z., Kazakov, A., and Dryer, F. 2004. An updated comprehensive kinetic model of hydrogen combustion. *Int. J. Chem. Kinetics*, **36**(10), 566–575.

Masri, A.R., Dibble, R.W., and Barlow, R.S. 1996. The structure of turbulent nonpremixed flames revealed by Raman-Rayleigh-LIF measurements. *Prog. Energy Combust. Sci*., **22**, 307–362.

Meier, W., Prucker, S., Cao, M.-H., and Stricker, W. 1996. Characterization of turbulent H_2/N_2/air jet diffusion flames by single-pulse spontaneous raman scattering. *Combust. Sci. Technol*., **118**, 293–312.

Miles, P.C., and Barlow, R.S. 2000. A fast mechanical shutter for spectroscopic applications. *Measure. Sci. Technol*., **11**, 392–397.

Neuber, A., Krieger, G., Tacke, M., Hassel, E., and Janicka, J. 1998. Finite rate chemistry and NO mole fraction in non-premixed turbulent flames. *Combust. Flame*, **113**, 198–211.

Pfuderer, D.G., Neuber, A.A., Früchtel, G., Hassel, E.P., and Janicka, J. 1996. Turbulence modulation in jet diffusion flames: Modeling and experiments. *Combust. Flame*, **106**, 301–317.

Sutton, G., Levick, A., Edwards, G., and Greenhalgh, D. 2006. A combustion temperature and species standard for the calibration of laser diagnostic techniques. *Combust. Flame*, **147**(1–2), 39–48.

Weiland, N.T., Chen, R.-H., and Strakey, P.A. 2011. Effects of coaxial air on nitrogen-diluted hydrogen jet diffusion flame length and NOx emission. *Proc. Combust. Inst*., **33**(2), 2983–2989.

Weiland, N.T., Sidwell, T.G., and Strakey, P.A. 2010. Effect of pressure and air preheating on dilute hydrogen jet diffusion flames with coaxial air injection. In *Proceedings of the* 2010 *Technical Meeting of the Central States Section of The Combustion Institute*, Champaign, IL, March 21–23.

Weiland, N.T., and Strakey, P.A. 2007a. Stability regimes of turbulent nitrogen-diluted hydrogen jet flames. In *Proceedings of the 5th US National Meeting of the Combustion Institute*, San Diego, CA, March 25–28.

Weiland, N.T., and Strakey, P.A. 2007b. Global NOx measurements in turbulent nitrogen-diluted hydrogen jet flames. In *Proceedings of the 5th US National Meeting of the Combustion Institute*, San Diego, CA, March 25–28.

Weiland, N.T., and Strakey, P.A. 2009. Stability characteristics of turbulent hydrogen dilute diffusion flames. *Combust. Sci. Technol*., **181**, 756–781.

Weiland, N.T., and Strakey, P.A. 2010. NOx reduction by air-side versus fuel-side dilution in hydrogen diffusion flame combustors. *J. Eng. Gas Turbines Power*, **132**(7), 071504.